Full Length Article

Dry reforming of methane using modified sodium and protonated titanate nanotube catalysts

Wesley F. Monteiro[a], Michele O. Vieira[a], Camila O. Calgaro[b], Oscar W. Perez-Lopez[b,c], Rosane A. Ligabue[a,d,]*

[a] Graduate Program in Materials Engineering and Technology, Pontifical Catholic University of Rio Grande do Sul – PUCRS, Brazil
[b] Graduate Program in Chemical Engineering, Federal University of Rio Grande do Sul – UFRGS, Brazil
[c] School of Engineering, Federal University of Rio Grande do Sul – UFRGS, Brazil
[d] School of Sciences, Pontifical Catholic University of Rio Grande do Sul – PUCRS, Brazil

GRAPHICAL ABSTRACT
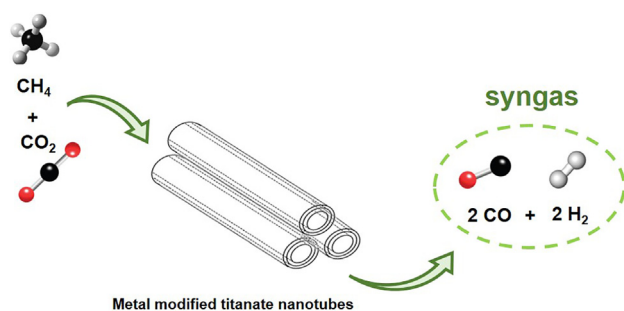
Metal modified titanate nanotubes

ARTICLE INFO

ABSTRACT

The mitigation of carbon emissions is an imminent and extremely relevant issue. In addition to carbon dioxide (CO_2), methane (CH_4) also contributes significantly to climate change. Dry reforming of methane (DRM) is a promising alternative to mitigate this gas, generating syngas, an important precursor of several chemical routes. In this context, sodium and protonated titanate nanotubes (TNT) were modified with metals (Co, Cu, Zn and Ni) and evaluated as catalyst for DRM. Zn-NaTNT, Co-NaTNT and Cu-NaTNT showed low catalytic activity (CO_2 and CH_4 conversion < 5%). However, when Ni-NaTNT and Ni-HTNT were used as catalyst, CO_2 and CH_4 conversions were of 35 and 27% (Ni-NaTNT) and 70 and 74% (Ni-HTNT), respectively. Both catalysts showed good stability keeping CO_2 and CH_4 conversions at 700 °C during 5 h of reaction. Additionally, although conversion values reached with Ni-NaTNT were lower, the sodium presence in this catalyst inhibits to coke formation when compared to Ni-HTNT.

1. Introduction

In recent years, the concentration of greenhouse gases (GHG) in the atmosphere has increased at an alarming rate due to anthropogenic activities such as the burning of fossil fuels to generate energy [1]. Carbon dioxide (CO_2) is the most detrimental greenhouse gas to environmental and it reached an concentration record of 411 ppm in 2019 [2,3]. Gases found in lower concentrations, such as methane (CH_4),

nitrogen oxides (NO_x) and volatile organic compounds (VOCs), also contribute significantly to climate change [3,4]. Faced with this scenario, there is significant global mobilization to reduce emissions of these gases. In 2017, the United Nations Climate Change Conference in Bonn (Germany) found that despite efforts and planning to lower CO_2 emissions, the average temperature of the planet is still 2 °C above the ideal and could increase to 3 °C by 2020 [5]. On the other hand, the US, followed by Canada and China, are the leading producers of shale gas [6], with a production that increased more than 30% in the last 10 years [7]. Methane (CH_4), the major component of shale gas, plays a significant role in global warming [8]. According to the Intergovernmental Panel on Climate Change [9], urgent changes are needed to mitigate carbon emissions, since it is estimated that climate change could lead to a 10% decline in the annual GDP growth rate of developing countries by the end of century. In this context, research on the capture and conversion of greenhouse gases, primarily CO_2 and CH_4, is highly relevant and essential to reducing their environmental impact [10–14].

Methane reforming technologies include steam methane reforming (SMR), partial oxidation (POM) and dry reforming of methane (DRM) [15]. Steam methane reforming (SMR) (Eq. (1)) is the most common route for industrial hydrogen production [16], the main disadvantage being the constant deactivation of catalysts [17] and high incidence of equipment corrosion [18] due to the presence of water. The main drawbacks of POM (Eq. (2)) are its high risk caused by the use of O_2 [19] and high cost owing to the origin of the gas (cryogenic air separation) [18]. Dry reforming of methane (DRM) (Eq. (3)) is a beneficial chemical process involving reaction between two primary greenhouse gases (methane and carbon dioxide) to produce hydrogen (H_2) and carbon monoxide (CO) [20].

$$CH_4 + H_2O \rightarrow CO + 3H_2 (\Delta H^{\circ}_{298\,K} = 228 kJ/mol) \qquad (1)$$

$$CH_4 + \tfrac{1}{2}O_2 \rightarrow CO + 2H_2 (\Delta H^{\circ}_{298K} = -22.6 kJ/mol) \qquad (2)$$

$$CH_4 + CO_2 \rightarrow 2CO + 2H_2 (\Delta H^{\circ}_{298K} = 247\ kJ/mol) \qquad (3)$$
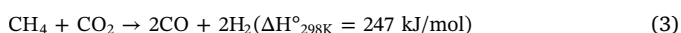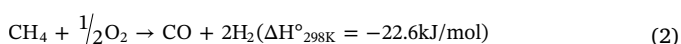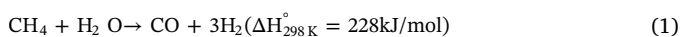
These methane-reforming products (CO and H_2) form a valuable gas mixture known as syngas. Syngas is an important precursor of several chemical routes, such as the conversion of synthetic fuels via the Fischer-Tropsch reaction, and methanol conversion into dimethyl ether and aromatic olefin [21,22]. The use of DRM enables the obtention of lower H_2/CO ratio, while SMR needs H_2/CO ratio > 3. A lower ratio can be preferentially used for production of liquid hydrocarbons in Fischer-Tropsch synthesis, while the high values inhibits the growth of the chain and decreases selectivity of higher hydrocarbons [23,24]. As disadvantage, DRM is affected by side reactions, such as methane decomposition (Eq. (4)), reverse water-gas shift (RWGS, Eq. (5)) and Boudouard reaction (Eq. (6)) that aid carbon formation and deposition on catalyst [25].

$$CH_4 \rightleftharpoons C + 2H_2 (\Delta H^{\circ}_{298K} = 75\ kJ/mol) \qquad (4)$$

$$CO_2 + H_2 \rightleftharpoons CO + 2H_2O (\Delta H^{\circ}_{298K} = 41 kJ/mol) \qquad (5)$$

$$CO \rightleftharpoons C + CO_2 (\Delta H^{\circ}_{298K} = -173\ kJ/mol) \qquad (6)$$
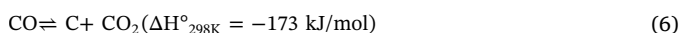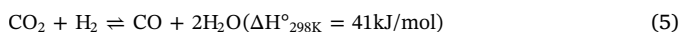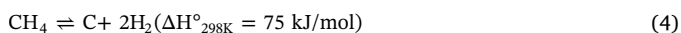
In addition for increasing syngas yield and quality, DRM requires stable catalysts because of the high reaction temperatures (600–900 °C). Catalyst deactivation due to sintering and the formation of a carbon layer (coke) is a significant concern [26]. This coke formation originates from the contribution of the different side reactions such as Boudouard reaction (Eq. (6)) might lead to structural degradation and deactivation [27]. A detailed study showed that carbon deposition can be originated by both CH_4 decomposition (Eq. (4)) and carbon monoxide disproportionation (Eq. (6)) [28]. The CH_4 decompositions reactions leading to formation of C^* in a series of elementary H-abstraction steps [29]. As H atoms are abstraction from CH_4, this step become faster and chemisorbed carbon is then removed using CO_2 [30].

Nanostructured catalysts modified with metals such as mixed

cerium and lanthanum oxides [31], $Ni-Al_2O_3$ modified with La, Ce and Zr [32] and, Rh-based catalysts [33] have been studied as alternatives to minimize the barriers in DRM. However, the high cost associated to these catalysts synthesis can be a disadvantage. With the same purpose, metals such as copper, zinc, cobalt and nickel have been used to modify nanostructures, such as perovskite and magnesium or zirconium oxide, among others [34–38]. Several studies have used different catalysts in methane reforming, and systems based on Ni nanoparticles have shown promising results. Phan et al. (2018) and Daoura et al. (2018) developed catalysts based on hydroxyapatite modified with cobalt/nickel-containing mesocellular silica foam [39,40]. The reactions occurred at 700 °C and the catalytic systems presented an excellent CH_4 conversion results (approximately 80%), presented higher stability after 20 h of reactions [39,40]. Furthermore, Zhang et al. (2018) studied nanostructured catalysts with nickel nanoparticles embedded in AlSBA-15 mesopores [41]. The results obtained were higher than 60% of CH_4 conversion using 700 °C as reaction temperature and good catalyst stability after 5 h of reaction [41].

One of the problems encountered in DRM reaction is the deactivation of the catalyst by coke formation, that is dependent of temperature [42]. Studies are showed that the use of supports with basic characteristics or modified with basic promoters (alkali and alkaline earths metal oxides) help in adsorption and activation of CO_2 species on the catalysts, suppressing the carbon formation through CO disproportionation, making it an interesting strategy [43]. Shiraz, Rezaei and Meshkani (2016) showed that modification of Ni/Al_2O_3 catalyst with K, Mg, Ca and Ba, reduced the coke formation when compared with unmodified catalyst [44]. In a recent publication, Zhang et al. (2018) evaluated the influence of MgO in the Ni/SiO_2 catalyst [45]. The results showed that the catalyst modified presented a high reduction on the coke formation.

Within this context, titanate nanotubes (TNT), nanostructures synthesized from titanium dioxide nanoparticles (TiO_2) using a simple low-cost hydrothermal method [46], are potential catalysts for DRM. Classic titanate nanotubes present Na atoms (NaTNT), in their structure, or by acid wash process, are converted in its protonated form (HTNT). TNT have a large specific surface area and high concentration of active sites [47]. Due to this, TNT have been shown to be efficient catalysts in a variety of reactions, including PET glycolysis [48], biodiesel synthesis [49], acetylation of glycerol [50], among others. Besides that, some works, including previous work from our group, showed that NaTNT can adsorbed and activate CO_2 molecule [51,52].

Coelho et al. studied sodium titanate nanotubes as support for Ni, Pt and Co and their activity to DRM [53]. The better results were obtained in 600 °C using TNT modified with Ni reaching 25% of CH_4 conversion. However, no study about the influence of sodium in the nanostructure was reported. In this context, the present study aims to enrich debate in DRM area evaluating the interaction of different metals (Co, Cu, Zn and Ni) with TNTs as support and applying these catalysts to DRM reaction. In addition, the focus is evaluating the influence of presence or not of sodium atoms in TNT nanostructure in relation to coke formation.

2. Methodology

2.1. Materials

For the synthesis of the catalysts, the following reactants were used as received: Sodium hydroxide, NaOH (Vetec, 99.0%), titanium dioxide, TiO_2 (JB Química, 98.0% anatase phase), zinc nitrate, Zn $(NO_3)_2 \cdot 6H_2O$ (Vetec, 99.0%), copper nitrate, $Cu(NO_3)_2 \cdot 3H_2O$ (Vetec, 99.0%), cobalt nitrate, $Co(NO_3)_2 \cdot 6H_2O$ (Vetec, 98.0%), nickel nitrate, $Ni(NO_3)_2 \cdot 6H_2O$ (Vetec, 97.0%) and hydrochloric acid, HCl (Anidrol, 37.0%v/v).

2.2. Catalysts syntheses

Sodium titanate nanotubes (NaTNT) were prepared according to the method described in the literature [54,55]. In a typical synthesis reaction, 1.5 g (18.8 mmol) of TiO_2 powder was mixed with 120 mL of 10 mol·L^{-1} NaOH solution under magnetic stirring for 30 min. Next, the suspension was hydrothermally treated in a 100 mL Teflon-lined autoclave at 130 °C for 72 h. The white precipitate obtained was washed with distilled water until pH = 7, then centrifuged and dried at 80 °C for 6 h. The NaTNTs were modified by wet impregnation [56]. Therefore, metallic aqueous solutions were prepared from 0.1 g of metallic salt (Zn, Cu, Co and Ni salts) in 50 mL of distilled water. Next, 1 g (3.3 mmol) of NaTNT was added in these solutions and the mix was kept under magnetic stirring at room temperature for 24 h. Lastly, the solid was dried at 80 °C for 12 h, and the nanostructures Zn-NaTNT, Cu-NaTNT, Co-NaTNT and Ni-NaTNT were obtained. Protonated titanate nanotubes (HTNT) were obtained from 1 g (3.3 mmol) of NaTNT mixed in an acid solution (HCl 0.5 mol·L^{-1}) for 30 min, washed with distilled water, centrifuged and dried at 80 °C for 6 h. Ni-HTNT was obtained from HTNT and a nickel nitrate solution, using the same procedure described above (impregnation with excess solvent). All the catalysts were calcined in a tubular quartz reactor with 50 mL·min^{-1} of synthetic air (21% O_2 and 79% N_2 v/v, White Martins, 99.997% of purity) and a heating rate of 10 °C·min^{-1}, from room temperature up to 600 °C for 2 h, as described in the literature [57].

2.3. Dry reforming of methane tests

The catalytic tests were performed in a fixed-bed quartz reactor (½ in. diameter) heated in an electric oven, under atmospheric pressure. Quartz wool was used to support the catalyst bed and silicon carbide as diluent. Temperature was measured using a K-type thermocouple and gas flow rates were established with digital mass flow controllers (Sierra Instruments). The flow rate used in the tests was 100 mL·min^{-1} at a CH_4:CO_2:N_2 volume ratio of 1:1:8. System pressure was monitored using a manometer. Runs were carried out at temperatures between 500 and 700 °C (molar ratio CO_2/CH_4 = 1). The products were analyzed by online gas chromatography (Varian 3600cx), with a packed column (Porapak Q), thermal conductivity detector, and N_2 as carrier gas.

Reaction runs were performed with approximately 100 mg of catalysts with GHSV of 12000 mL·g^{-1} h^{-1}. For reduced sample runs, the catalysts were activated *in situ* at 700 °C, under a mixture of H_2 and N_2 (100 mL·min^{-1}, volume ratio of 1:9, 10 °C·min^{-1}). Methane and carbon dioxide conversion were calculated according to Eq. (7) and (8), respectively. The H_2/CO ratios were estimated using Eq. (9).

$$CH_4 \text{ conversion}(\%) = \frac{(CH_{4(in)} - -CH_{4(out)})}{CH_{4(in)}} \times 100 \tag{7}$$

$$CO_2 \text{ conversion}(\%) = \frac{(CO_{2(in)} - -CO_{2(out)})}{CO_{2(in)}} \times 100 \tag{8}$$

$$H_2/CO \text{ ratio} = \frac{H_{2(out)}}{CO_{(out)}} \tag{9}$$

2.4. Characterization of catalysts

All characterizations were performed using powdered calcined catalysts. Morphological analysis of the nanostructured catalysts was performed by field emission scanning electron microscopy (FESEM, FEI Inspect F50) in secondary electron beam and dispersive energy spectroscopy (EDS) mode using 20 kV. The samples were coated with a thin gold film using ion beam sputtering. Transmission electron microscopy (TEM, FEI Tecnai G2 T20) was also used for morphological analysis, with samples deposited on 300 mesh carbon film coated copper grids.

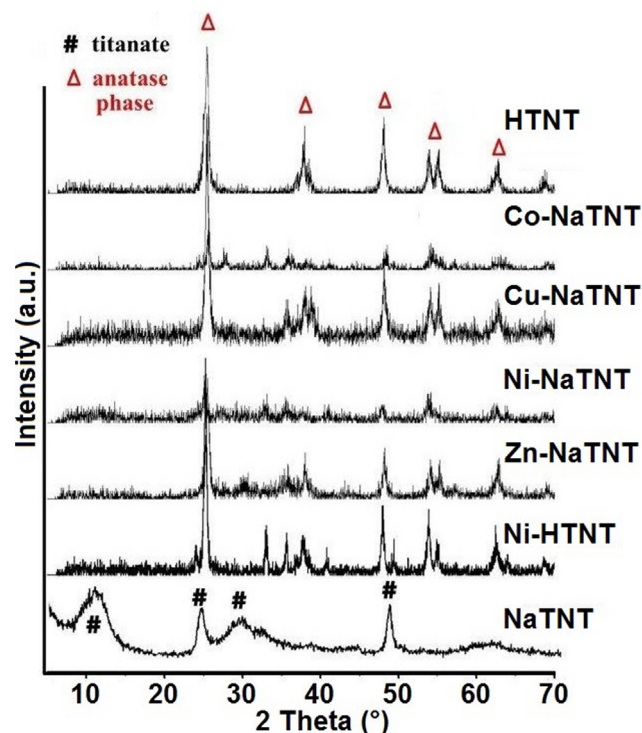Temperature-programmed reduction (TPR) analyses were

Fig. 1. XRD results of calcined samples.

performed in a multipurpose system (SAMP3), at a heating rate of 10 °C·min^{-1} up to 850 °C, under a H_2:N_2 mixture (1:9 vol ratio), with a total flow rate of 30 mL·min^{-1}.

Thermogravimetric analyses (TGA) and temperature programmed oxidation (TPO) were conducted in an SDT Q600 device (TA Instruments) at a heating rate of 10 °C·min^{-1} from room temperature to 800 °C, under air flow.

X-ray diffraction (XRD) patterns were obtained for the fresh and spent catalysts using a BRUKER D2-Phaser diffractometer under Cu-Ka radiation, at 30 kV and 10 mA.

3. Results and discussion

3.1. Catalyst properties

The XRD patterns for calcined catalysts are shown in Fig. 1. The NaTNT nanostructure exhibits characteristic diffraction peaks for lamellar titanate structures at 2θ = 10°, 24°, 28°, 48° and 62° [50,51], while HTNT shows peaks at 2θ = 25.4°, 37.8°, 48.0°, 53.8°, 55.1° and 69°, similar to described in the literature and in agreement with anatase XRD patterns [52]. The Cu-NaTNT samples presented small peaks between 35 and 39° related to CuO phase, whereas, additional peaks at 33, 35.7 and 49.5° in Ni-HTNT are ascribed to nickel titanate ($NiTiO_3$) phase [58]. These peaks are smaller for Ni-NaTNT, indicating a smaller crystallites size.

H_2-TPR analyses were performed to investigate the reducibility of the calcined samples and interaction between different metal particles and the support. The results are presented in Fig. 2. A peak was observed above 700 °C for the Co-NaTNT nanostructure, corresponding to Co_3O_4 reduction ($Co^{3+} \rightarrow Co^{2+} \rightarrow Co^0$) with strong interaction with support, which is well described in the literature [57]. In the present study, this peak at high temperature indicating that cobalt showed a strong interaction with the NaTNT when compared to others supports, like alumina [59] and silica [60], that showed reduction peaks below 500 °C. On the other hand, Cu-NaTNT showed a single intense peak at low temperature (maximum ≈ 300 °C), related to the reduction of CuO species that exhibit weak interaction with the support [61,62]. No
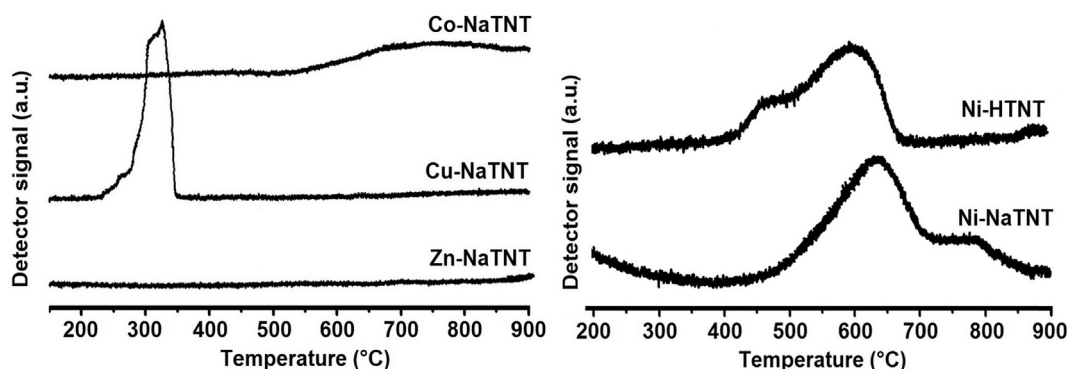
Fig. 2. TPR results for different nanostructure catalysts.

reduction signal was observed for the Zn-NaTNT nanostructure, but an interesting behavior was noted for the Ni-NaTNT and Ni-HTNT catalysts. The first exhibited two peaks, one at 630 °C, corresponding to NiO_x reduction ($NiO \rightarrow Ni°$), showing strong interaction with the support (NaTNT), and another at 790 °C, which may be associated with the reduction of Ni in the NaTNT structure or small crystals of NiO that are difficult to reduce. The first signal for Ni-HTNT is located at 450 °C and can be attributed to the reduction of NiO_x species in a weaker interaction with the tubular structure. The second signal (600 °C) is associated with the reduction of small Ni from $NiTiO_3$ [63–65].

This behavior can be better assessed by deconvolution the TPR profiles (Fig. 3). Deconvolution of the TPR profiles for the Ni-NaTNT and Ni-HTNT samples showed three peaks corresponding to NiO reduction to Ni^0, where the rise in temperature is related to greater interaction between NiO and support [65]. Rui et al. (2014) also reported strong interaction between NiO species and TiO_2 [66] and to the $NiTiO_3$ formation. Fig. 3 indicates that the reduction temperatures of the deconvoluted peaks were significantly lower for the Ni-HTNT sample than for Ni-NaTNT, indicating the higher interaction of the Ni particles with support in this last nanostructure. This interaction can be favored by the migration of Na^+ to the Ni particles, which will difficult the diffusion of hydrogen [64,67,68].

TEM images for Co-NaTNT and Zn-NaTNT presented difference when compared with Cu and Ni-NaTNT (Fig. 4). In some parts are observed metal free nanotubes and small particle agglomerates (Fig. 4). Distribution of nanoparticles were similar when compared the Cu-NaTNT, Ni-NaTNT and Ni-HTNT nanostructures. EDS mapping obtained from SEM images (Fig. 4) for Co (blue), Cu (red) and Zn (purple) showed signs of metal atoms in all the samples. The Ni-NaTNT and Ni-HTNT nanostructures exhibited a homogeneous nanoparticle distribution over the nanotubes (Fig. 4).

These results present a contribution about the modification of

titanate nanotubes with some low cost metals. Use of classic impregnation method to modify the support with Zn and Co generated a heterogeneous distribution of nanoparticles over the nanotubes. Modification with Cu nanoparticles although having homogeneous distribution, has a low reduction temperature, showing weak interaction with support. Ni nanoparticles were shown a homogeneous distribution and great interaction with support.

3.2. Catalytic activity in DRM reactions

Temperature is an important parameter for this reaction due to their endothermic nature [25] and as such, the influence of this parameter in NaTNT and HTNT nanostructures was assessed first. NaTNT exhibited low activity, not exceeding 11% CO_2 conversion and 13% CH_4 conversion, whereas HTNT displayed negligible CO_2 and CH_4 conversion rates. The Co-NaTNT, Cu-NaTNT and Zn-NaTNT catalysts showed very low activity (CO_2 and CH_4 conversion < 5%) (Fig. 5). The low activity observed for the Co and Zn catalysts can be attributed to the hard reducibility of the catalyst, as observed in TPR analysis (Fig. 2) which will not produce active metals. In the case of Cu-NaTNT, this metal has a lower interaction with support, evidenced by TPR analyses. This easy reducibility can lead to the agglomeration of the metal particles, which can result in the low catalytic activity [34]. Ni-NaTNT was the best catalyst among the samples using NaTNT as support, exhibiting greater CO_2 and CH_4 conversion with an increase in the reaction temperature (35% and 27% at 700 °C, respectively). For this catalyst, CO_2 conversion was slightly higher than CH_4 conversion due to the reverse water–gas shift reaction ($CO_2 + H_2 \rightarrow CO + H_2O$, RWGS) that occurs in DRM [69].

In light of these results, only Ni was used to modify the protonated titanate nanotubes (HTNT). Results obtained with Ni-HTNT were far higher than those observed with Ni-NaTNT nanostructure. CO_2 and CH_4
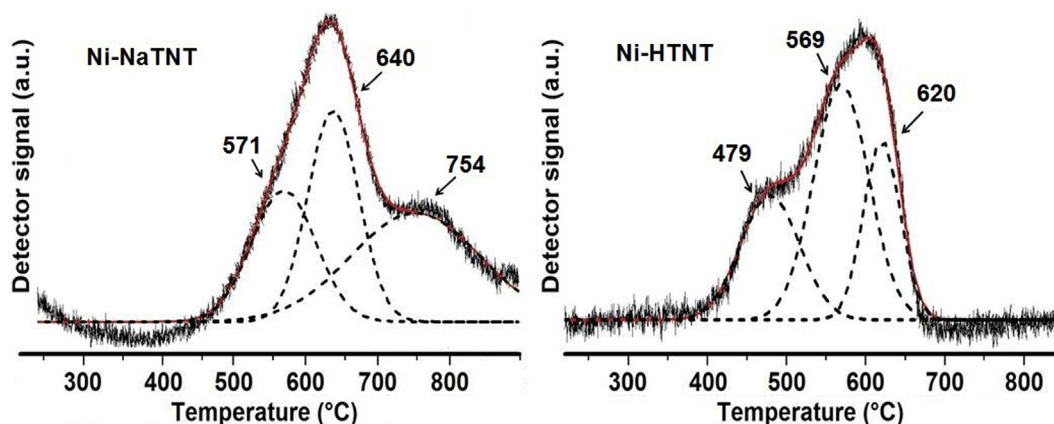

Fig. 3. Deconvolution of TPR profiles for Ni-NaTNT and Ni-HTNT nanostructure.
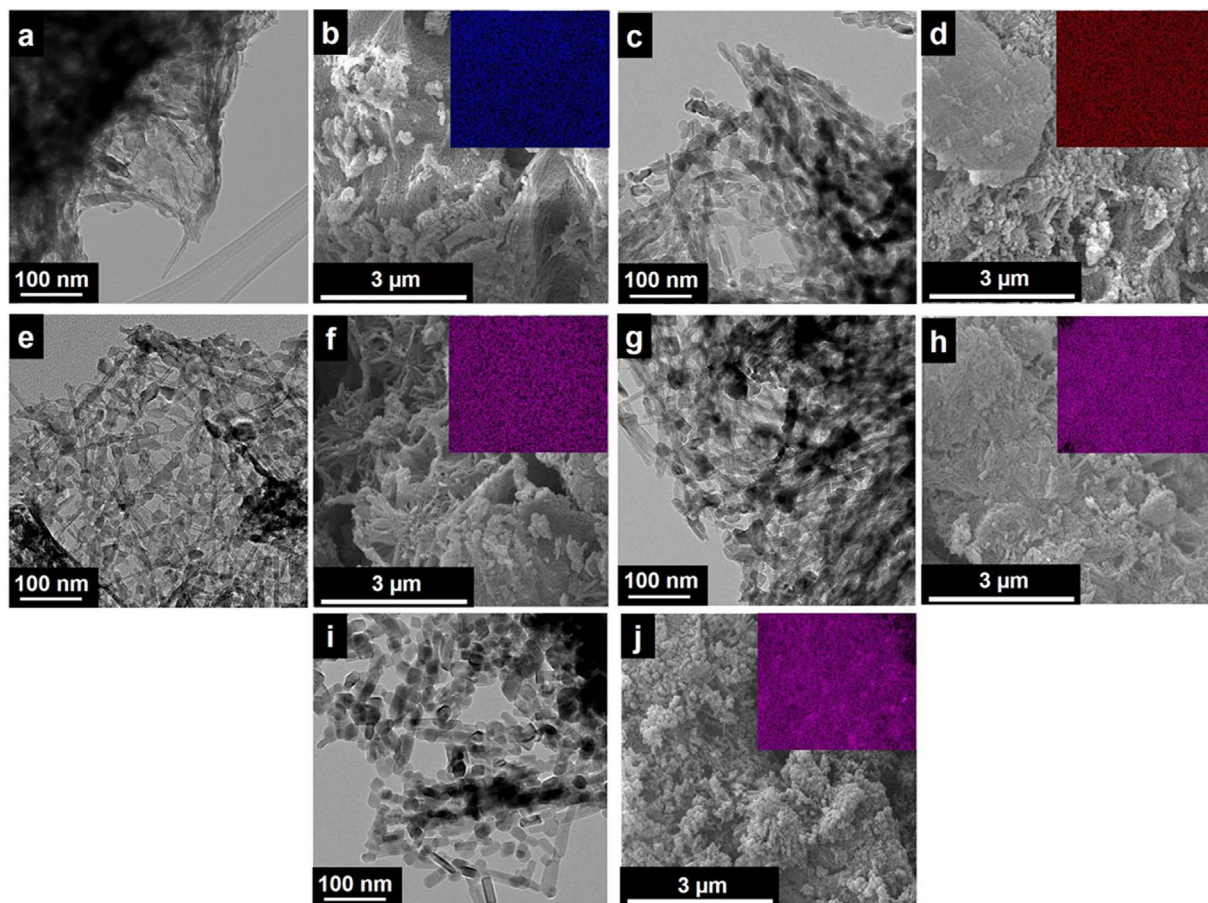
Fig. 4. TEM and SEM images, respectively of (a, b) Co-NaTNT, (c, d) Cu-NaTNT, (e, f) Zn-NaTNT, (g, h) Ni-NaTNT and (i, j) Ni-HTNT. EDS are presented in each SEM image.

conversion were 47 and 41% at 600 °C, respectively, and reaching 70 and 74% of CO_2 and CH_4 conversion at 700 °C. Our results, compared to literature [53] showed that the protonation of nanostructure of the support leading to the improve in their catalytic activity.

A lower activity observed to Ni-NaTNT can be associated to the smaller crystallite size of Ni nanoparticles or due to their interaction with Na^+, as observed in TPR analyzes. Only the Ni-HTNT catalyst approaches the equilibrium conversion of CH_4 and CO_2 at the higher temperatures evaluated [70]. The Ni-HTNT catalyst led to a linear increase in CH_4 and CO_2 conversion according to the increase of the temperature. However, for the Ni-NaTNT catalyst, the proportional

increase of conversion to CH_4 and CO_2 occurs due to the DRM reaction, but this does not occur linearly with increasing temperature. The presence of Na in the Ni-NaTNT catalyst acts on carbon gasification during the reaction and influences the dispersion of the Ni in the catalyst.

The deactivation of DRM catalysts due to the formation of coke, which blocks the active metal sites been widely reported in literature [71]. As such, the stability tests for Ni-NaTNT and Ni-HTNT were performed at 700 °C (Fig. 6).

Fig. 6 shows that the catalysts remained stable after 5 h of reaction. The CO_2 and CH_4 conversion results were 45% for Ni-NaTNT and 79% for Ni-HTNT. A slight decline (< 5%) in conversion values was
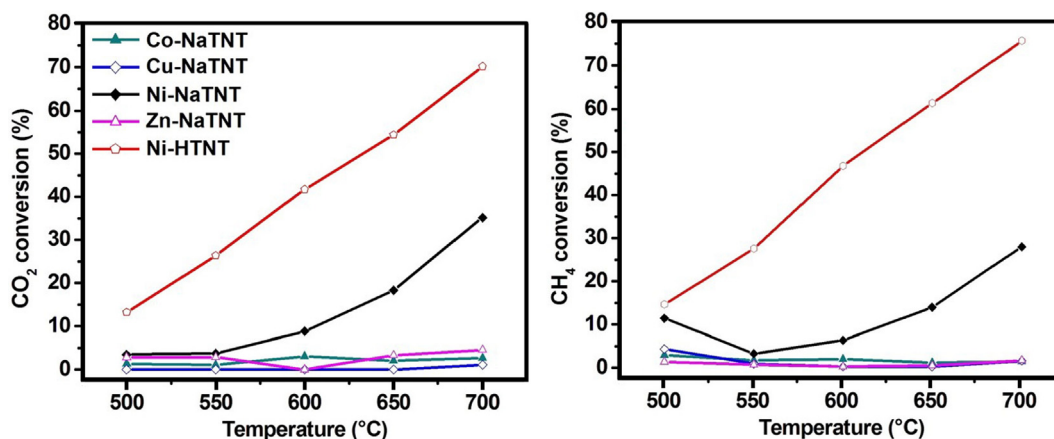

Fig. 5. Influence of reaction temperature on CO_2 and CH_4 conversion during DRM reactions.
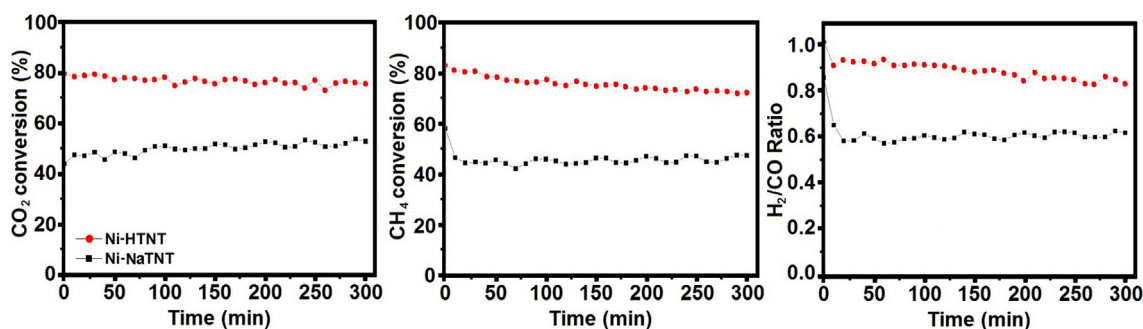
Fig. 6. Stability of Ni-NaTNT and Ni-HTNT catalysts in DRM reaction at 700 °C.

observed for Ni-HTNT, although its activity was noticeably superior to that of the Ni-NaTNT sample. The CH_4 conversion obtained Ni-HTNT it closes to the equilibrium conversion of 91.5%. In addition, CO_2 conversion for HTNT it is higher than equilibrium conversion (66.7%) [70]. The favoring of the reverse water gas shift reaction (RWGS) may increase the conversion of CO_2 depending on the catalyst and conditions used. The H_2/CO ratios for Ni-NaTNT and Ni-HTNT were approximately 0.6 and 0.8, respectively. Low values also suggest inhibition of the reverse water gas shift reaction (RWGS) [72].

The activity differences between Ni-NaTNT and Ni-HTNT are related to the particle size formed. Ni-HTNT sample present relatively large Ni particles and, consequently, are more easily reduced resulting in high activity. At the same time, these particles present lower stability, because there is slight loss of activity over time. On the other hand, the Ni particles are smaller in Ni-NaTNT and more difficult to reduce, consequently this sample shows lower initial activity but there is an increase in activity over time. These results are in agreement with the XRD pattern (Fig. 1) and TPR profiles (Fig. 2) for these samples.

3.3. Spent catalyst characterization and coke formation

Coke formation was initially assessed based on the XRD patterns of spent catalysts (Fig. 7). The spent catalysts exhibited new diffraction peaks at $2\theta = 27°$ and $44°$. The diffraction peak at $27°$ was attributed to the carbon produced during DRM [45], whereas the peaks at $44°$ is related to metallic Ni. A comparison of the spent Ni-NaTNT and Ni-HTNT samples demonstrated that the more intense peak carbon diffraction peak for Ni-HTNT suggests greater carbon deposition. On the other hand, the carbon peak for Ni-NaTNT was small, indicating that this sample had greater resistance to carbon formation when compared
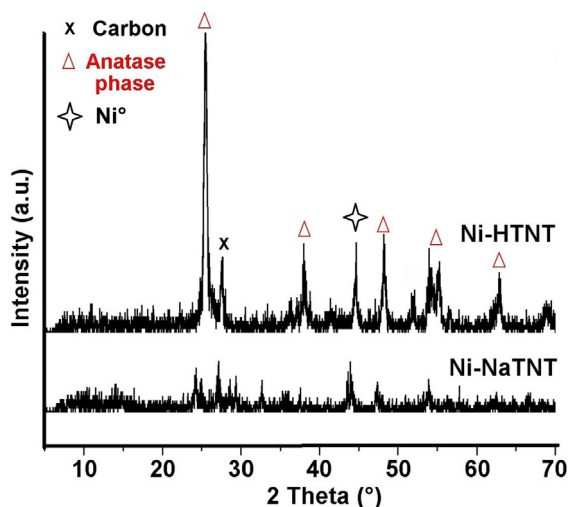
to Ni-HTNT, which can be attributed to the presence of Na^+ in the support nanostruture. In addition, the peak at $44°$ is more intense an narrower for Ni-HTNT indicating large Ni^0 crytallite size than Ni-NaTNT and suggesting sintering of Ni^0 particles.

TGA and TPO analysis of spent catalysts was also used to evaluate the amount of carbon produced in DRM. According to Fig. 8a, Ni-NaTNT exhibited only a small weight increase between 300 and 400 °C, corresponding to the oxidation of nickel particles supported on the spent catalysts [73,74]. However, weight loss ($\approx 21\%$) was also observed for Ni-HTNT between 500 and 650 °C, due to the oxidation of carbon deposited on the catalyst. The TPO (Fig. 8b) results for both catalysts indicated oxidation at lower temperatures (< 400 °C), corresponding to the activated carbon also called amorphous carbon [69,71]. Considering the low weight variation in this range, the amount of amorphous carbon was small and similar for both samples. Additionally, an intense peak was observed at 580 °C for Ni-HTNT, attributed to filamentous carbon or carbon nanotube oxidation [75]. The TPO results corroborate the findings of XRD, demonstrating low carbon deposition in Ni-NaTNT nanostructures and that using NaTNT as support may suppress carbon formation on the Ni surface.

The SEM and TEM images of the spent catalysts are shown in Fig. 9. Three types of carbons are commonly reported in the literature, *i.e.*: (i) amorphous carbon, (ii) graphitic carbon and (iii) carbon nanotubes [57]. As shown in the TPO and XRD analyses, the Ni-NaTNT nanostructure (Figs. 7 and 8) does not favor carbon deposition in the form of carbon filaments, but rather a low level of amorphous carbon. The morphology of spent catalysts after 300 min of reaction showed nanoparticles homogeneously dispersed on the nanotubes and covered by amorphous carbon (Fig. 9c, d). Fig. 9d shows small dark spots on the catalysts associated with the sintering of Ni nanoparticles at high temperatures, similar to behavior described in literature [71]. The SEM and TEM images of Ni-HTNT are presented in Fig. 9(e–h), indicating the presence of carbon filaments (Fig. 9h) around the Ni nanoparticles formed by multiple walls. In both reactions, with the Ni-NaTNT and Ni-HTNT catalyst, through the TEM images (Fig. 9c and d) the crystallite sintering of Ni is observed.

The presence of Na^+ in the nanostructure of Ni-NaTNT confers coking resistance properties when compared to Ni-HTNT, evident in the low carbon content observed in TPO analyses. Dry methane reforming involves CH_4 decomposition followed by carbon species oxidation. The DRM mechanism requires metal-supported catalysts capable of catalyzing CH_4 adsorption and decomposition and hindering or removing carbon species. In a recent study, Dama et al. (2018) found that the presence of alkaline earth metals such as calcium (Ca) in the bimetallic catalyst $MZr_{1-x}Ni_xO_{3-\delta}$ resulted in high coking resistance [76]. This effect is similar to that obtained by the presence of Na in the support.

3.4. Proposed schematic diagram for Ni-NaTNT and Ni-HTNT

A schematic diagram of the catalytic system was proposed (Fig. 10) based on the results obtained in this study. The first step corresponds to
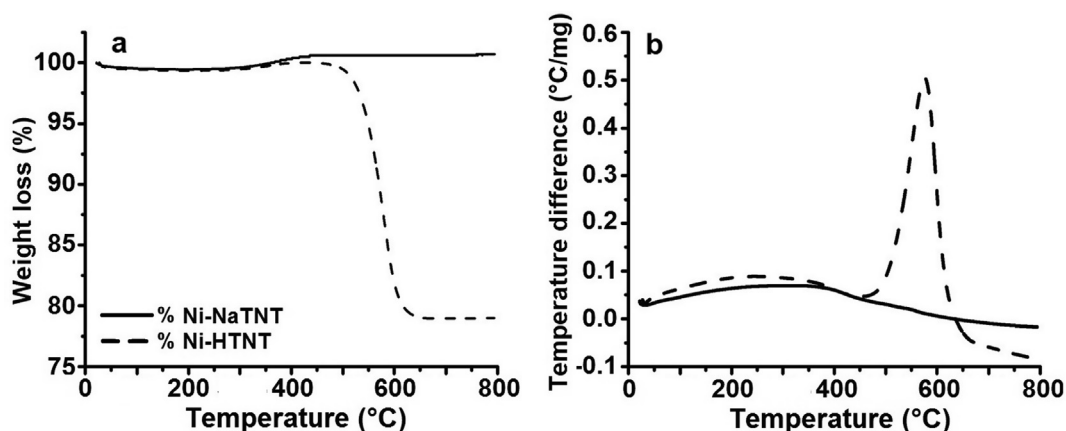

Fig. 7. XRD results of the spent Ni-NaTNT and Ni-HTNT catalysts.

Fig. 8. (a) Thermogravimetric analysis and (b) TPO results for Ni-NaTNT and Ni-HTNT catalysts.
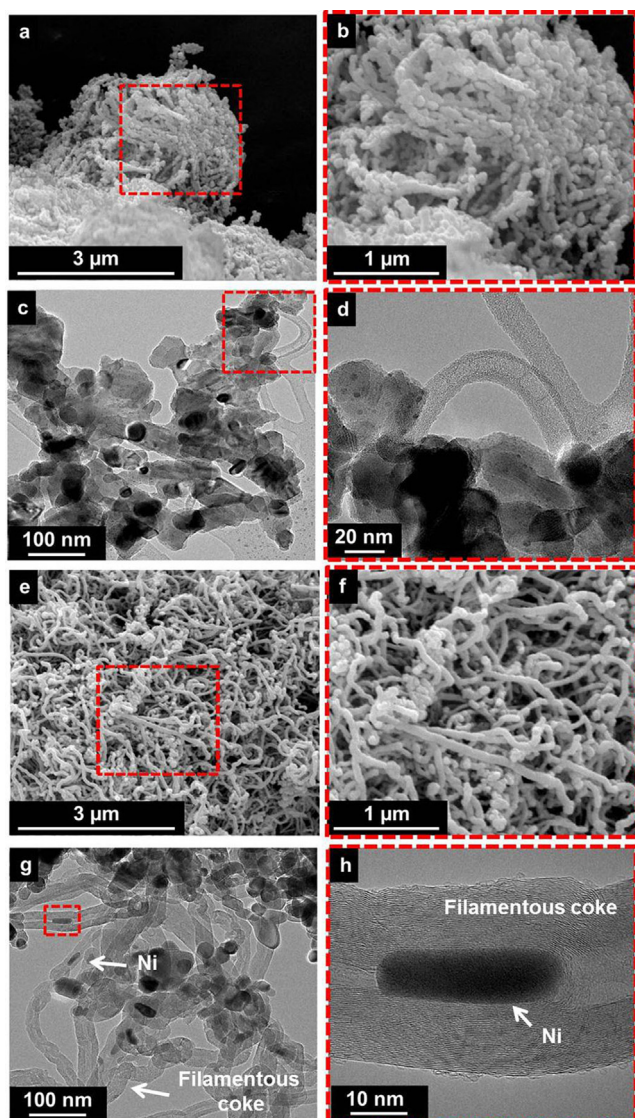

Fig. 9. Results of spent catalyst to Ni-NaTNT analyzed by SEM (a, b), TEM (c, d) and to Ni-HTNT analyzed by SEM (e, f) and TEM (g, h).

CH_4 activation and dissociation on the surface of Ni nanoparticles to form CH_x and H species [29]. These species when combined, leave the surface as H_2 [76,77]. The TNTs exhibit good interaction and CO_2 activation capacity due to the presence of acid and basic sites in the nanostructure [51,52,78–80]. As such, the second step corresponds to CO_2 adsorption and decomposition on the TNT surface to form CO species. The Ni-HTNT catalyst showed carbon formation. The carbon deposition occurs from CH_4 decomposition in a series of elementary H-abstraction steps that is not removed by desorption or reaction with chemisorbed O^* derived from CO_2 or H_2O co-reactants [29]. The accumulation separates the Ni nanoparticles from the support. This occurs because the growth of carbon nanotubes around the nanoparticles toward the exterior of the catalyst causes Ni nanoparticles to separate from the support, as shown in Fig. 9g, h. However, some Ni nanoparticles remain active for the reaction.

The Ni-NaTNT nanostructure displayed good coking resistance, without the presence filamentous carbon when compared to Ni-HTNT. This effect can be explained by the presence of Na^+ ions in the nanostructure, which can migrate from the support to nickel particles, inhibiting coke formation. By contrast, the interaction of Na^+ and Ni nanoparticles may reduce the active sites, thereby lowering conversion values [67,68]. The change of Na^+ by H^+ improves the actives sites in the titanate nanotubes, in special acid sites [81,82]. Thus, a part of CH_4 molecules can interact with support, which will increase the conversion.

4. Conclusion

This study presented the synthesis and characterization of sodium and protonated titanate nanotubes (NaTNT and HTNT, respectively) modified with metals (Co, Cu, Zn and Ni). TPR analyzes showed high interaction of Ni with the support, while Cu presented easy reducibility. Ni-NaTNT and Ni-HTNT catalysts proved to be highly efficient in DRM. In this study was evidenced that the presence of sodium in the nanostructure of the support, although present decreased the activity of the catalyst, provided resistance to coke formation. HTNT when used as support provide a catalyst with greater activity, however, the formation of carbon filamentous its observed.

In summary, the Ni-HTNT catalyst exhibits higher activity due to the larger size of the Ni particles, which in turn are easily activated but present formation of carbon filaments. On the other hand, the Ni-NaTNT catalyst presents a smaller crystallite size but is more difficult to activate and consequently with less activity but with high stability and resistance to carbon deposition.

Acknowledgments
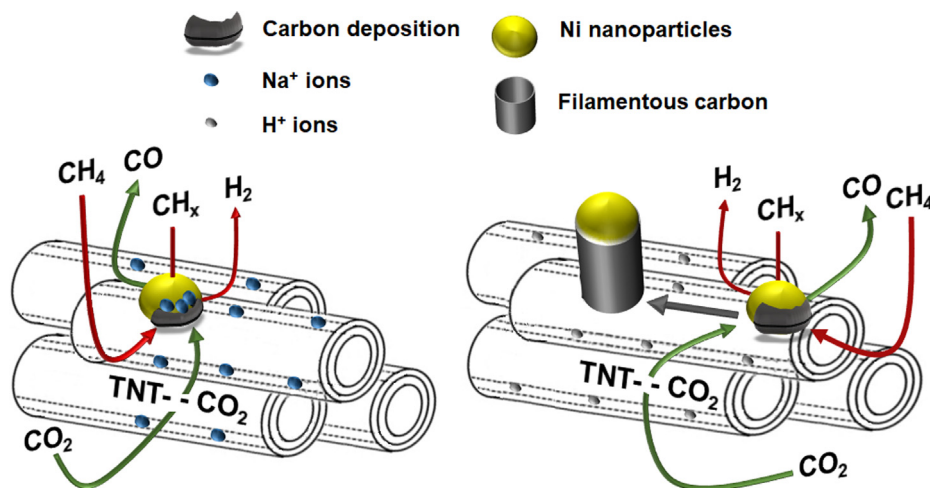
Fig. 10. Schematic diagram of the DRM catalyzed by Ni-NaTNT (left) and Ni-HTNT (right).

References

[1] Zoundi Z. CO₂ emissions, renewable energy and the Environmental Kuznets Curve, a panel cointegration approach. Renew Sustain Energy Rev 2017;72:1067–75. https://doi.org/10.1016/j.rser.2016.10.018.

[2] NOAA, National Oceanic and Atmospheric Administration. https://www.noaa.gov/, 2019 (accessed May 01, 2019).

[3] EPA, United States Environmental Protection Agency. https://nepis.epa.gov, 2012 (accessed May 01, 2019).

[4] Hoehne CG, Chester MV. Greenhouse gas and air quality effects of auto first-last mile use with transit. Transp Res Part D Transp Environ 2017;53:306–20. https://doi.org/10.1016/j.trd.2017.04.030.

[5] COP23, 23rd Conference of the Parties to the United Nations Framework Convention on Climate Change. Bonn – Alemanha. https://unfccc.int/prior-your-arrival-z (accessed 15 august 2018).

[6] Yu CH, Huang SK, Qin P, Chen X. Local residents' risk perceptions in response to shale gas exploitation: Evidence from China. Energy Policy 2018;113:123–34. https://doi.org/10.1016/j.enpol.2017.10.004.

[7] Bădileanu M, Bulearcă MFR, Russu C, Muscalu M-S, Neagu C, Bozga R, et al. Shale gas exploitation– Economic effects and risks. Procedia Econ Finance 2015;22:95–104. https://doi.org/10.1016/S2212-5671(15)00231-2.

[8] Cui G, Liu J, Wei M, Feng X, Elsworth D. Evolution of permeability during the process of shale gas extraction. J Nat Gas Sci Eng 2018;49:94–109. https://doi.org/10.1016/j.jngse.2017.10.018.

[9] IPCC (2014). Climate Change 2014: Impacts, Adaptation, and Vulnerability. Contribution of Working Group II to the Fifth Assessment Report of the Intergovernmental Panel on Climate Change. Cambridge: Cambridge University Press. 2014.

[10] Aquino AS, Bernard FL, Vieira MO, Borges JV, Rojas MF, Vecchia FD, et al. A new approach to CO₂ capture and conversion using imidazolium based-ionic liquids as sorbent and catalyst. J Braz Chem Soc 2014;25:2251–7. https://doi.org/10.5935/0103-5053.20140176.

[11] Cuéllar-Franca RM, Azapagic A. Carbon capture, storage and utilisation technologies: a critical analysis and comparison of their life cycle environmental impacts. J CO₂ Util 2015;9:82–102. https://doi.org/10.1016/j.jcou.2014.12.001.

[12] Aquino AS, Bernard FL, Borges JV, Mafra L, Vecchia FD, Vieira MO, et al. Rationalizing the role of the anion in CO₂ capture and conversion using imidazolium-based ionic liquid modified mesoporous silica. RSC Adv 2015;5:64220–7. https://doi.org/10.1039/C5RA07561K.

[13] Vieira MO, Aquino AS, Schütz MK, Vecchia FD, Ligabue R, Seferin M, et al. Chemical conversion of CO₂: evaluation of different ionic liquids as catalysts in dimethyl carbonate synthesis. Energy Procedia 2017;114:7141–9. https://doi.org/10.1016/j.egypro.2017.03.1876.

[14] Vieira MO, Monteiro WF, Neto BS, Ligabue R, Chaban VV, Einloft S. Surface active ionic liquids as catalyst for CO₂ conversion to propylene carbonate. Catal Letters 2018;148. https://doi.org/10.1007/s10562-017-2212-4.

[15] Abdullah B, Abd Ghani NA, Vo DVN. Recent advances in dry reforming of methane over Ni-based catalysts. J Clean Prod 2017;162:170–85. https://doi.org/10.1016/j.jclepro.2017.05.176.

[16] Fan J, Zhu L, Jiang P, Li L, Liu H. Comparative exergy analysis of chemical looping combustion thermally coupled and conventional steam methane reforming for hydrogen production. J Clean Prod 2016;131:247–58. https://doi.org/10.1016/j.jclepro.2016.05.040.

[17] Carvalho LS, Martins AR, Reyes P, Oportus M, Albonoz A, Vicentini V, et al. Preparation and characterization of Ru/MgO-Al₂O₃ catalysts for methane steam reforming. Catal Today 2009;142:52–60. https://doi.org/10.1016/j.cattod.2009.01.010.

[18] Djinović P, Osojnik črnivec IG, Erjavec B, Pintar A. Influence of active metal loading and oxygen mobility on coke-free dry reforming of Ni-Co bimetallic catalysts. Appl Catal B Environ 2012;125:259–70. https://doi.org/10.1016/j.apcatb.2012.05.049.

[19] Asencios YJO, Assaf EM. Combination of dry reforming and partial oxidation of methane on NiO-MgO-ZrO₂ catalyst: Effect of nickel content. Fuel Process Technol 2013;106:247–52. https://doi.org/10.1016/j.fuproc.2012.08.004.

[20] Aramouni NAK, Touma JG, Tarboush BA, Zeaiter J, Ahmad MN. Catalyst design for dry reforming of methane: analysis review. Renew Sustain Energy Rev 2018;82:2570–85. https://doi.org/10.1016/j.rser.2017.09.076.

[21] Barelli L, Bidini G, Gallorini F, Servili S. Hydrogen production through sorption-enhanced steam methane reforming and membrane technology: a review. Energy 2008;33:554–70. https://doi.org/10.1016/j.energy.2007.10.018.

[22] Bahari MB, Phuc NHH, Abdullah B, Alenazey F, Vo DVN. Ethanol dry reforming for syngas production over Ce-promoted Ni/Al₂O₃ catalyst. J Environ Chem Eng 2016;4:4830–8. https://doi.org/10.1016/j.jece.2016.01.038.

[23] Ghoneim SA, El-Salamony RA, El-Temtamy SA. Review on innovative catalytic reforming of natural gas to syngas. World J Eng Technol 2016;04:116–39. https://doi.org/10.4236/wjet.2016.41011.

[24] Touahra F, Chebout R, Lerari D, Halliche D, Bachari K. Role of the nanoparticles of Cu-Co alloy derived from perovskite in dry reforming of methane. Energy 2019;171:465–74. https://doi.org/10.1016/j.energy.2019.01.085.

[25] Abdulrasheed A, Jalil AA, Gambo Y, Ibrahim M, Hambali HU, Shahul Hamid MY. A review on catalyst development for dry reforming of methane to syngas: recent advances. Renew Sustain Energy Rev 2019;108:175–93. https://doi.org/10.1016/j.rser.2019.03.054.

[26] Jeong MG, Kim SY, Kim DH, Han SW, Kim IH, Lee M, et al. High-performing and durable MgO/Ni catalysts via atomic layer deposition for CO₂ reforming of methane (CRM). Appl Catal A Gen 2016;515:45–50. https://doi.org/10.1016/j.apcata.2016.01.032.

[27] Horváth A, Stefler G, Geszti O, Kienneman A, Pietraszek A, Guczi L. Methane dry reforming with CO₂ on CeZr-oxide supported Ni, NiRh and NiCo catalysts prepared by sol-gel technique: relationship between activity and coke formation. Catal Today 2011;169:102–11. https://doi.org/10.1016/j.cattod.2010.08.004.

[28] Gili A, Schlicker L, Bekheet MF, Görke O, Penner S, Grünbacher M, et al. Surface carbon as a reactive intermediate in dry reforming of methane to syngas on a 5% Ni/MnO Catalyst. ACS Catal 2018;8:8739–50. https://doi.org/10.1021/acscatal.8b01820.

[29] Wei J, Iglesia E. Structural requirements and reaction pathways in methane activation and chemical conversion catalyzed by rhodium. J Catal 2004;225:116–27. https://doi.org/10.1016/j.jcat.2003.09.030.

[30] Wei J, Iglesia E. Isotopic and kinetic assessment of the mechanism of reactions of CH₄ with CO₂ or H₂O to form synthesis gas and carbon on nickel catalysts. J Catal 2004;224:370–83. https://doi.org/10.1016/j.jcat.2004.02.032.

[31] Wang M, Zhao T, Dong X, Li M, Wang H. Effects of Ce substitution at the A-site of LaNi₀.₅Fe₀.₅O₃ perovskite on the enhanced catalytic activity for dry reforming of methane. Appl Catal B Environ 2018;224:214–21. https://doi.org/10.1016/j.apcatb.2017.10.022.

[32] Rahbar Shamskar F, Meshkani F, Rezaei M. Preparation and characterization of ultrasound-assisted co-precipitated nanocrystalline La-, Ce-, Zr -promoted Ni-Al₂O₃ catalysts for dry reforming reaction. J CO₂ Util 2017;22:124–34. https://doi.org/10.1016/j.jcou.2017.09.014.

[33] Moral A, Reyero I, Alfaro C, Bimbela F, Gandía LM. Syngas production by means of biogas catalytic partial oxidation and dry reforming using Rh-based catalysts. Catal Today 2018;299:280–8. https://doi.org/10.1016/j.cattod.2017.03.049.

[34] Sutthiumporn K, Maneerung T, Kathiraser Y, Kawi S. CO2 dry-reforming of methane over La0.8Sr0.2Ni0.8M0.2O3 perovskite (M = Bi Co, Cr, Cu, Fe): roles of lattice oxygen on C-H activation and carbon suppression. Int J Hydrogen Energy 2012;37:11195–207. https://doi.org/10.1016/j.ijhydene.2012.04.059.

[35] Song K, Lu M, Xu S, Chen C, Zhan Y, Li D, et al. Effect of alloy composition on catalytic performance and coke-resistance property of Ni-Cu/Mg(Al)O catalysts for dry reforming of methane. Appl Catal B Environ 2018;239:324–33. https://doi.org/

10.1016/j.apcatb.2018.08.023.

[36] Mirzaei F, Rezaei M, Meshkani F, Fattah Z. Carbon dioxide reforming of methane for syngas production over Co-MgO mixed oxide nanocatalysts. J Ind Eng Chem 2015;21:662–7. https://doi.org/10.1016/j.jiec.2014.03.034.

[37] Moradi GR, Rahmanzadeh M. Khosravian F. The effects of partial substitution of Ni by Zn in LaNiO3 perovskite catalyst for methane dry reforming. J CO$_2$ Util 2014;6:7–11. https://doi.org/10.1016/j.jcou.2014.02.001.

[38] Park JH, Yeo S, Kang TJ, Shin HR, Heo I, Chang TS. Effect of Zn promoter on catalytic activity and stability of Co/ZrO$_2$ catalyst for dry reforming of CH$_4$. J CO$_2$ Util 2018;23:10–9. https://doi.org/10.1016/j.jcou.2017.11.002.

[39] Phan TS, Sane AR, Rêgo de Vasconcelos B, Nzihou A, Sharrock P, Grouset D, et al. Hydroxyapatite supported bimetallic cobalt and nickel catalysts for syngas production from dry reforming of methane. Appl Catal B Environ 2018;224:310–21. https://doi.org/10.1016/j.apcatb.2017.10.063.

[40] Daoura O, Kaydouh MN, El-Hassan N, Massiani P, Launay F, Boutros M. Mesocellular silica foam-based Ni catalysts for dry reforming of CH$_4$ (by CO$_2$). J CO$_2$ Util 2018;24:112–9. https://doi.org/10.1016/j.jcou.2017.12.010.

[41] Zhang X, Zhang L, Peng H, You X, Peng C, Xu X, et al. Nickel nanoparticles embedded in mesopores of AlSBA-15 with a perfect peasecod-like structure: A catalyst with superior sintering resistance and hydrothermal stability for methane dry reforming. Appl Catal B Environ 2018;224:488–99. https://doi.org/10.1016/j.apcatb.2017.11.001.

[42] Jang WJ, Jeong DW, Shim JO, Kim HM, Roh HS, Son IH, et al. Combined steam and carbon dioxide reforming of methane and side reactions: thermodynamic equilibrium analysis and experimental application. Appl Energy 2016;173:80–91. https://doi.org/10.1016/j.apenergy.2016.04.006.

[43] Kawi S, Kathiraser Y, Ni J, Oemar U, Li Z, Saw ET. Progress in synthesis of highly active and stable nickel-based catalysts for carbon dioxide reforming of methane. ChemSusChem 2015;8:3556–75. https://doi.org/10.1002/cssc.201500390.

[44] Shiraz MHA, Rezaei M, Meshkani F. The effect of promoters on the CO$_2$ reforming activity and coke formation of nanocrystalline Ni/Al$_2$O$_3$ catalysts prepared by microemulsion method. Korean J Chem Eng 2016;33:3359–66. https://doi.org/10.1007/s11814-016-0203-6.

[45] Zhang Q, Feng X, Liu J, Zhao L, Song X, Zhang P, et al. Hollow hierarchical Ni/MgO-SiO$_2$ catalyst with high activity, thermal stability and coking resistance for catalytic dry reforming of methane. Int J Hydrogen Energy 2018;43:11056–68. https://doi.org/10.1016/j.ijhydene.2018.05.010.

[46] Erjavec B, Kaplan R, Pintar A. Effects of heat and peroxide treatment on photocatalytic activity of titanate nanotubes. Catal Today 2015;241:15–24. https://doi.org/10.1016/j.cattod.2014.04.005.

[47] Camposeco R, Castillo S, Mejia-Centeno I, Navarrete J, Rodriguez-Gonzalez V. Behavior of lewis and Brönsted surface acidity featured by Ag, Au, Ce, La, Fe, Mn, Pd, Pt, V and W decorated on protonated titanate nanotubes. Microporous Mesoporous Mater 2016;236:235–43. https://doi.org/10.1016/j.micromeso.2016.08.033.

[48] Lima GR, Monteiro WF, Ligabue R, Santana RMC. Titanate nanotubes as new nanostrutured catalyst for depolymerization of PET by glycolysis reaction. Mater Res 2017;20:588–95. https://doi.org/10.1590/1980-5373-mr-2017-0645.

[49] Hernández-Hipólito P, García-Castillejos M, Martínez-Klimova E, Juárez-Flores N, Gómez-Cortés A, Klimova ET. Biodiesel production with nanotubular sodium titanate as a catalyst. Catal Today 2014;220–222:4–11. https://doi.org/10.1557/adv.2015.52.

[50] de Carvalho DC, Oliveira AC, Ferreira OP, Filho JM, Tehuacanero-Cuapa S, Oliveira AC. Titanate nanotubes as acid catalysts for acetalization of glycerol with acetone: influence of the synthesis time and the role of structure on the catalytic performance. Chem Eng J 2017;313:1454–67. https://doi.org/10.1016/j.cej.2016.11.047.

[51] Monteiro WF, Vieira MO, Aquino AS, de Souza MO, de Lima J, Einloft S, et al. CO$_2$ conversion to propylene carbonate catalyzed by ionic liquid containing organosilane groups supported on titanate nanotubes/nanowires. Appl Catal A Gen 2017;544:46–54. https://doi.org/10.1016/j.apcata.2017.07.011.

[52] Chen A, Zhao T, Gao H, Chen L, Chen J, Yu Y. Titanate nanotube-promoted chemical fixation of carbon dioxide to cyclic carbonate: a combined experimental and computational study. Catal Sci Technol 2016;6:780–90. https://doi.org/10.1039/C5CY01024A.

[53] Coelho DC, Oliveira AC, Filho JM, Oliveira AC, Lucredio AF, Assaf EM, et al. Effect of the active metal on the catalytic activity of the titanate nanotubes for dry reforming of methane. Chem Eng J 2016;290:438–53. https://doi.org/10.1016/j.cej.2016.01.051.

[54] Monteiro WF, dos Santos CAB, Einloft S, Oberson M, Carone CLP, Ligabue RA. Preparation of modified titanate nanotubes and its application in polyurethane nanocomposites. Macromol Symp 2016;368:93–7. https://doi.org/10.1002/masy.201500146.

[55] Monteiro WF, Santos CAB, Hoffmann MS, Carone CLP, Einloft SMO, De Souza MO, et al. Modified titanate nanotubes for the production of novel aliphatic polyurethane nanocomposites. Polym Compos 2018:1–9. https://doi.org/10.1002/pc.25038.

[56] Munnik P, de Jongh PE, de Jong KP. Recent developments in the synthesis of supported catalysts. Chem Rev 2015;115:6687–718. https://doi.org/10.1021/cr500486u.

[57] Calgaro CO, Perez-Lopez OW. Decomposition of methane over Co$_{3−x}$Al$_x$O$_4$(x = 0–2) coprecipitated catalysts: the role of Co phases in the activity and stability. Int J Hydrogen Energy 2017;42:29756–72. https://doi.org/10.1016/j.ijhydene.2017.10.082.

[58] Kumar BS, Shanmugharaj AM, Kalpathy SK, Anandhan S. Some new observations on the structural and phase evolution of nickel titanate nanofibers. Ceram Int 2017;43:6845–57. https://doi.org/10.1016/j.ceramint.2017.02.105.

[59] Wang HY, Ruckenstein E. Conversions of methane to synthesis gas over Co/γ -Al$_2$O$_3$ by CO$_2$ and/or O$_2$. Catal Lett 2001;75:13–8. https://doi.org/10.1023/A:1016719703118.

[60] Li H, Li J, Ni H, Song D. Studies on cobalt catalyst supported on silica with different pore size for Fischer-Tropsch synthesis. Catal Lett 2006;110:71–6. https://doi.org/10.1007/s10562-006-0086-y.

[61] Nataj SMM, Alavi SM, Mazloom G. Modeling and optimization of methane dry reforming over Ni-Cu/Al$_2$O$_3$ catalyst using Box-Behnken design. J Energy Chem 2017:1–14. https://doi.org/10.1016/j.jechem.2017.10.002.

[62] Tahay P, Khani Y, Jabari M, Bahadoran F, Safari N. Highly porous monolith/TiO$_2$ supported Cu, Cu-Ni, Ru, and Pt catalysts in methanol steam reforming process for H$_2$ generation. Appl Catal A Gen 2018;554:44–53. https://doi.org/10.1016/j.apcata.2018.01.022.

[63] Benrabaa R, Barama A, Boukhlouf H, Guerrero-Caballero J, Rubbens A, Bordes-Richard E, et al. Physico-chemical properties and syngas production via dry reforming of methane over NiAl$_2$O$_4$ catalyst. Int J Hydrogen Energy 2017;42:12989–96. https://doi.org/10.1016/j.ijhydene.2017.04.030.

[64] Gurav HR, Dama S, Samuel V, Chilukuri S. Influence of preparation method on activity and stability of Ni catalysts supported on Gd doped ceria in dry reforming of methane. J CO$_2$ Util 2017;20:357–67. https://doi.org/10.1016/j.jcou.2017.06.014.

[65] Berndt FM, Perez-Lopez OW. Catalytic decomposition of methane over Ni/SiO$_2$: influence of Cu addition. React Kinet Mech Catal 2017;120:181–93. https://doi.org/10.1007/s11144-016-1096-4.

[66] Rui Z, Feng D, Chen H, Ji H. Anodic TiO$_2$ nanotube array supported nickel e noble metal bimetallic catalysts for activation of CH$_4$ and CO$_2$ to syngas. Int J Hydrogen Energy 2014;39:16252–61. https://doi.org/10.1016/j.ijhydene.2013.10.150.

[67] Castro Luna AE, Iriarte ME. Carbon dioxide reforming of methane over a metal modified Ni-A$_2$O$_3$ catalyst. Appl Catal A Gen 2008;343:10–5. https://doi.org/10.1016/j.apcata.2007.11.041.

[68] Snoeck J-W, Froment GF, Fowles M. Steam/CO$_2$ reforming of methane. Carbon formation and gasification on catalysts with various potassium contents. Ind Eng Chem Res 2002;41:3548–56. https://doi.org/10.1021/ie010665p.

[69] Park JH, Yeo S, Kang TJ, Heo I, Lee KY, Chang TS. Enhanced stability of Co catalysts supported on phosphorus-modified Al$_2$O$_3$ for dry reforming of CH$_4$. Fuel 2018;212:77–87. https://doi.org/10.1016/j.fuel.2017.09.090.

[70] Nikoo MK, Amin NAS. Thermodynamic analysis of carbon dioxide reforming of methane in view of solid carbon formation. Fuel Process Technol 2011;92:678–91. https://doi.org/10.1016/j.fuproc.2010.11.027.

[71] Zhang Q, Zhang T, Shi Y, Zhao B, Wang M, Liu Q, et al. A sintering and carbon-resistant Ni-SBA-15 catalyst prepared by solid-state grinding method for dry reforming of methane. J CO$_2$ Util 2017;17:10–9. https://doi.org/10.1016/j.jcou.2016.11.002.

[72] Izquierdo-Colorado A, Dębek R, Da Costa P, Gálvez ME. Excess-methane dry and oxidative reforming on Ni-containing hydrotalcite-derived catalysts for biogas upgrading into synthesis gas. Int J Hydrogen Energy 2018:1–9. https://doi.org/10.1016/j.ijhydene.2018.04.237.

[73] Li X, Li D, Tian H, Zeng L, Zhao ZJ, Gong J. Dry reforming of methane over Ni/La$_2$O$_3$ nanorod catalysts with stabilized Ni nanoparticles. Appl Catal B Environ 2017;202:683–94. https://doi.org/10.1016/j.apcatb.2016.09.071.

[74] Perez-Lopez OW, Senger A, Marcilio NR, Lansarin MA. Effect of composition and thermal pretreatment on properties of Ni-Mg-Al catalysts for CO$_2$ reforming of methane. Appl Catal A Gen 2006;303:234–44. https://doi.org/10.1016/j.apcata.2006.02.024.

[75] Zardin L, Perez-Lopez OW. Hydrogen production by methane decomposition over Co-Al mixed oxides derived from hydrotalcites: Effect of the catalyst activation with H$_2$ or CH$_4$. Int J Hydrogen Energy 2017;42:7895–907. https://doi.org/10.1016/j.ijhydene.2017.02.153.

[76] Dama S, Ghodke SR, Bobade R, Gurav HR, Chilukuri S. Active and durable alkaline earth metal substituted perovskite catalysts for dry reforming of methane. Appl Catal B Environ 2018;224:146–58. https://doi.org/10.1016/j.apcatb.2017.10.048.

[77] Du X, Zhang D, Shi L, Gao R, Zhang J. Morphology dependence of catalytic properties of Ni/CeO$_2$ nanostructures for carbon dioxide reforming of methane. J Phys Chem C 2012;116:10009–16. https://doi.org/10.1021/jp300543r.

[78] Ntho TA, Anderson JA, Scurrell MS. CO oxidation over titanate nanotube supported Au: deactivation due to bicarbonate. J Catal 2009;261:94–100. https://doi.org/10.1016/j.jcat.2008.11.009.

[79] Liu Y, Liu J, Yao W, Cen W, Wang H, Weng X, et al. The effects of surface acidity on CO$_2$ adsorption over amine functionalized protonated titanate nanotubes. RSC Adv 2013;3:18803–10. https://doi.org/10.1039/c3ra42597e.

[80] Tang Q, Sun Z, Wang P, Li Q, Wang H, Wu Z. Enhanced CO$_2$ photocatalytic reduction performance on alkali and alkaline earth metal ion-exchanged hydrogen titanate nanotubes. Appl Surf Sci 2019;463:456–62. https://doi.org/10.1016/j.apsusc.2018.08.245.

[81] Lima GR, Monteiro WF, Scheid CM, Ligabue RA, Santana RMC. Evaluation of sodium/protonated titanate nanotubes catalysts in virgin and post consumer PET depolymerization. Catal Lett 2019;149:1415–26. https://doi.org/10.1007/s10562-019-02724-8.

[82] Lorençon E, Alves DCB, Krambrock K, Ávila ES, Resende RR, Ferlauto AS, et al. Oxidative desulfurization of dibenzothiophene over titanate nanotubes. Fuel 2014;132:53–61. https://doi.org/10.1016/j.fuel.2014.04.020.